

Hierarchical Object Parsing from Noisy Point Clouds

Adrian Barbu*

Abstract

Object parsing and segmentation from point clouds are challenging tasks because the relevant data is available only as thin structures along object boundaries or other object features and is corrupted by large amounts of noise. One way to handle this kind of data is by employing shape models that can accurately follow the object boundaries. Popular models such as Active Shape and Active Appearance models lack the necessary flexibility for this task. While more flexible models such as Recursive Compositional Models have been proposed, this paper builds on the Active Shape models and makes three contributions. First, it presents a flexible, mid-entropy, hierarchical generative model of object shape and appearance in images. The input data is explained by an object parsing layer, which is a deformation of a hidden PCA shape model with Gaussian prior. Second, it presents a novel efficient inference algorithm that uses a set of informed data-driven proposals to initialize local searches for the hidden variables. Third, it applies the proposed model and algorithm to object parsing from point clouds such as edge detection images, obtaining state of the art parsing errors on two out of three standard datasets without using any intensity information.

1. Introduction

Object parsing and segmentation are important problems with many applications in computer vision and medical imaging. While object segmentation is only directed towards extracting the object boundary, object parsing is aimed at identifying the object parts such as head, body, legs, etc. Active Shape and Active Appearance models [6] are popular methods that can address both object segmentation and object parsing. The Active Shape Models (ASM) contain a PCA shape model and alternate one step that searches for local boundary evidence on the shape normals with an

other step that reprojects the evidence onto the PCA plane, until convergence. The ASM method only uses partial image information existent on the shape normals and its result depends on initialization. In the Active Appearance models (AAM), the object appearance is also modeled by PCA and a trained iterative algorithm takes an initial shape towards the solution, guided by the image. The AAM uses more image information than the ASM, but the result is still dependent on initialization.

Another limitation of the ASM/AAM models is the lack in accuracy, as a low dimensional PCA shape cannot accurately describe the shape variability existent in real images, and is limited only to the main deformations. This is illustrated in Figure 1, where a 10-dimensional PCA shape shown in green cannot accurately follow the horse boundary and is off by a few pixels around the ears, back, legs, etc.

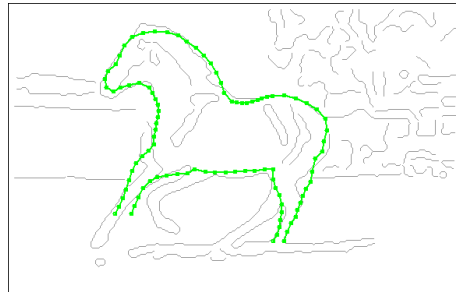


Figure 1. Motivation for the hierarchical model. A shape described by PCA (shown with green dots) is not flexible enough to accurately follow the object boundary, but can serve as a backbone to limit the variability of the model.

The approach introduced in this paper brings three contributions to object parsing and segmentation.

First, it presents a hierarchical generative model that represents the object shape as a MRF-based deformation from a PCA backbone, obtaining a higher degree of accuracy than just the PCA model. If desired, sample shapes can be extracted from the generative model and can be used for integration or to compute marginal statistics. The shape model is completed with a data term that connects the image information with the current object shape. Due to the high accuracy of the shape description, this model can be used for object parsing from point clouds (such as those obtained

*A. Barbu is with the Department of Statistics, Florida State University, Tallahassee, Florida 32306, USA, Phone: 850-980-2516, Fax: 850-644-5271, Email: abarbu@stat.fsu.edu.

from edge detection), where the data information is one pixel wide.

A second contribution is the optimization algorithm for finding a strong optimum for the hierarchical model. The algorithm uses a data-driven set of PCA candidates to initialize local searches for the deformation and PCA parameters. The proposed shape model and inference algorithm could in principle be adapted for other object parsing and segmentation applications by using other data terms, or even by using more accurate backbone shape models than the PCA.

The third contribution is the application of the proposed approach to parsing horses, cows and faces from point clouds. An evaluation on Weizmann horses [4], cows [13] and faces [24] shows that the proposed algorithm obtains state of the art results on two of the datasets without using any intensity information.

2. Related Work

One of the most representative works in object parsing that can be applied to point clouds is the Recursive Compositional Models (RCM) [31]. RCM represents the object shape in a hierarchical fashion using multiple levels of rotation-invariant models based on triplets of elements. The first level elements are the detected image edges, while the elements for each subsequent level are summaries of the triplets from the previous level. Inference is obtained using a version of dynamic programming with pruning. In contrast, our hierarchical model represents the shape using a PCA model plus MRF deformations along the normals, and has only two levels in the hierarchy. Because of the high connectivity of our proposed model, exact inference algorithms based on dynamic programming are not applicable. Instead, we propose a smart search algorithm that makes local searches at a number of locations dictated by a bottom-up data-driven process. The advantage of our approach is the simplicity of the model, that can be easily learned from training examples. Our evaluation shows that the errors obtained by our approach are similar to the RCM, and that without using any image intensity information.

A robust hierarchical shape model was constructed for multi-view car alignment [15]. The model allows large deformations of the observed shape points and can also handle missing points due to occlusion or failures of the part detectors. Similar to our work, shape candidates are constructed from partial information obtained from part detectors to initialize a local search. However, these candidates have been directly generated using RANSAC, as the correspondence between the part detections and the model points was known. In the object parsing from point clouds, the

correspondence between input points and the object points is not known and the fraction of outliers is usually higher than 90%, making RANSAC computationally prohibitive (needing more than 10^6 candidates).

A related task to object parsing is object segmentation. In [31] a separate step based on intensity information is used to obtain the segmentation, while our approach obtains the segmentation without using any intensity information.

There is a large amount of work on region-based object segmentation [26, 28, 5, 14, 7, 27]. However, these works cannot be directly applied to object segmentation from point clouds where the data information is sparse and available only at the object boundaries.

Torresani et al, [26] model the shape as a rigid transformation plus PCA, without the MRF deformation from our formulation.

The work of Ren et al, [18] is targeted to object boundary detection. It does not obtain a clear object segmentation or a parsing into object parts. Furthermore, it uses both edge and gradient information as input data.

Felzenszwalb and Schwartz, [8] use a shape tree as a model and focus on shape matching and retrieval, without evaluating the parsing error.

Zhu et al, [32] use a circularity measure to find cycles with good continuations in edge detection images. However, it does not have any shape model so it addresses a different problem than ours.

The Active Skeleton [1] uses a skeleton-based shape model to detect objects from edge detection images. Even though in principle the method could be used for object parsing, it has not been evaluated for this purpose.

Interactive Object Segmentation with Graph Cuts [12] imposes a shape prior on a Graph Cut energy. However, the shape prior is based on a template with similarity transformation without any deformation and the Graph Cut energy is on pixels, so no object parsing or aligned boundary is obtained. This work was extended with a Kernel PCA shape prior [17], but still depending on manual initialization and obtaining just a segmentation without boundary alignment. In contrast, our method obtains object parsing and boundary alignment, hence not only the object boundary but also the object parts are obtained.

The knowledge based segmentation [3] uses a shape prior based on pairwise cliques between the shape points and a primal-dual algorithm for inference. In contrast, our framework uses a PCA-based model that cannot be decomposed in pairwise cliques and it could in principle be extended to work with non-linear shape models.

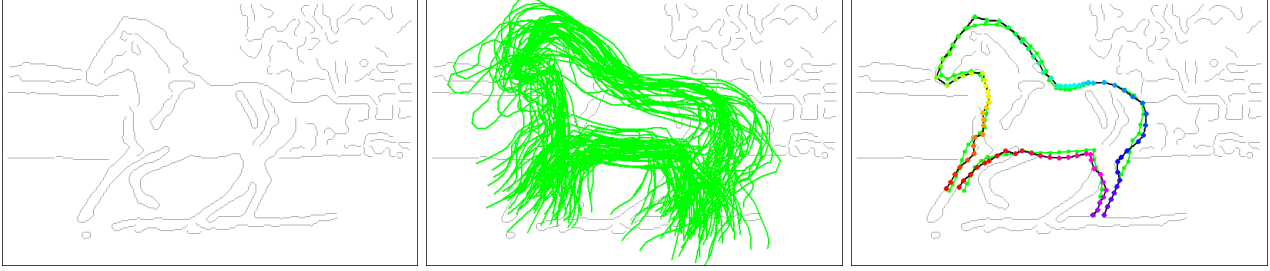


Figure 2. Our approach starts by tracing the points into chains (left), finds data-driven PCA candidates (middle) that are used to initialize local optimizations of the model parameters. The parameters of lowest energy give the parsing result (right, black with colored dots) and associated PCA shape (right, green).

Groups of nearby contour segments are used in [10, 21] to construct features for object detection. Our paper uses similar contour fragments to construct bottom-up data driven candidates for searching the shape space. The features from [10, 21] could be further used to obtain better discriminative object models. Currently we use a generative model, with some parameters trained in a discriminative manner.

The part-based constellation model from [23] uses an extension of the contour segment network from [10] to construct object parts and a Metropolis-Hastings stochastic algorithm for inference. However, the method is used for object detection, where the precise location of the boundary is not as important as in segmentation.

Another closely related work is the unsupervised learning of shape models [11], which uses pairs of adjacent contours [10] as features and a voting scheme to find the object parameters. A separate deformation step is then performed using Thin Plate Splines. In contrast, the inference algorithm from our work optimizes a single criterion that combines the shape and deformation into a single hierarchical model. Moreover, our work is aimed towards object parsing, whereas [11] is used for object and boundary detection.

The Active Basis Model [29] can obtain a sketch of an object using Gabor filters and has been successfully used for object detection. However, it has not been used for object segmentation, as it does not return a coherent object boundary.

Our approach is inspired by [9], where an efficient version of the Hough transform for line detection is obtained by voting at locations given by least squares line fitting of clusters of approximately collinear pixels.

Generating candidates based on partial information is similar to the beta channel from [30], where partially occluded faces are detected by combining eye, nose and mouth detections.

3. A Hierarchical Approach to Object Parsing

We propose a hierarchical generative model with two levels of hidden variables that need to be inferred from the input data. The first level C is the actual object parsing while the second level is a PCA shape model that limits the degree of variability of the first level.

The PCA shape is controlled by variables (A, β) consisting of a similarity transformation A and the PCA coefficients $\beta \in \mathbb{R}^p$. We abuse the notation by denoting A as both the transformation parameters $A = (u, v, s, \theta)$, with rotation θ , translation (dx, dy) and scale s , and the actual transformation

$$A(x, y) = (sx \cos \theta + sy \sin \theta + u, -sx \sin \theta + sy \cos \theta + v)$$

The PCA shape is

$$S(A, \beta) = A(\mu_x + P_x \beta, \mu_y + P_y \beta) = (S_1, \dots, S_N)' \quad (1)$$

where $\mu = (\mu_x, \mu_y)$, $\mu_x, \mu_y \in \mathcal{M}_{N,1}$ is the mean shape and $P = (P_x, P_y)$, $P_x, P_y \in \mathcal{M}_{N,p}$ are the PCA eigenvectors.

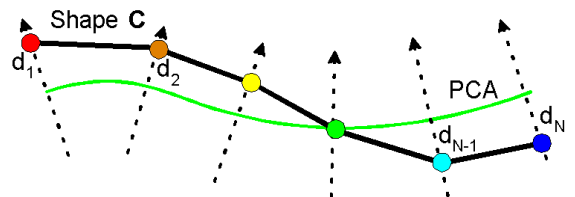


Figure 3. The shape C is obtained as a deformation $\mathbf{d} = (d_1, \dots, d_N)$ of a PCA shape (A, β) along the normals.

The representation is illustrated in Figure 3. The shape C (black) is obtained from the PCA shape (green) using a vector of displacements $\mathbf{d} = (d_1, \dots, d_N) \in [-d_{max}, d_{max}]^N$ along the normals to shape. More exactly, the shape $C = C(\mathbf{d})$ consists of a number of line segments $\overline{C_i, C_{i+1}}$ where $C_i = S_i + n_i d_i$, $i = 1, \dots, N$ and n_i is the normal to the PCA shape at S_i .

3.1. The Hierarchical Generative Model

The model can be represented either as a probability or an energy. For simplicity, we use an energy formulation of the model

$$E(C, A, \beta) = E_{data}(C) + E_{shape}(C, A, \beta) + E_p(A) \quad (2)$$

containing a data term $E_{data}(C)$ that relates the input data with the parsing result C , a shape term $E_{shape}(C, A, \beta)$ and a prior $E_p(A)$ on the possible transformations.

The data term $E_{data}(C)$ is application specific and is based on the exact location of the shape $C = (C_1, \dots, C_N)$. When the input data consists of noisy point clouds such as edge detection, the input points are traced into point chains based on the 8-neighborhood. The data term encourages consecutive points C_i, C_{i+1} to be on the same point chain:

$$E_{data}(C) = \sum_{i=1}^{N-1} \varphi(C_i, C_{i+1}) \quad (3)$$

where $\varphi(C_i, C_{i+1}) = -\delta$ if and only if C_i, C_{i+1} are on the same point chain and $\varphi(C_i, C_{i+1}) = 0$ otherwise.

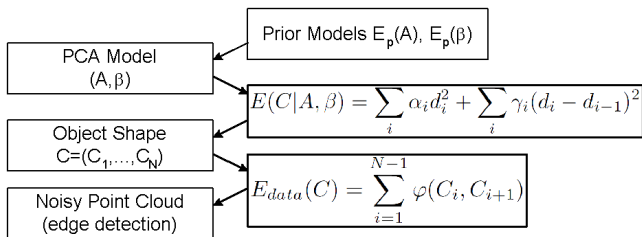


Figure 4. Diagram of the proposed hierarchical model.

The shape term

$$E_{shape}(C, A, \beta) = E(C|A, \beta) + E_p(\beta) \quad (4)$$

consists of a deformation term $E(C|A, \beta)$ that connects the parsed shape with the underlying PCA model and a prior $E_p(\beta)$ on the PCA coefficients.

The deformation term is a Gaussian MRF that encourages the curve (or curves) to be parallel and close to the PCA shape

$$E(C|A, \beta) = \sum_i \alpha_i d_i^2 + \sum_i \gamma_i (d_i - d_{i-1})^2 \quad (5)$$

and is defined in terms of the displacements d_i of the curve points C_i from the corresponding PCA shape points S_i . The coefficients α_i, γ_i represent the amount of penalty for the deformation at different points along the shape. In our applications all α_i have the same value $\alpha_i = \alpha$ and similarly $\gamma_i = \gamma$ but this could result in a decrease in model accuracy. For example the α_i

for points on the horse head could have smaller values because there is more variability for those points.

The prior $E_p(\beta)$ on the PCA parameters is a Gaussian prior based on the PCA eigenvalues λ_i

$$E_p(\beta) = \rho \sum_{i=1}^N \frac{\beta_i^2}{\lambda_i} \quad (6)$$

The prior $E_p(A)$ for $A = (u, v, s, \theta)$ forces the scale and rotation within a range and discourages translations away from the image center (x_c, y_c) :

$$E_p(A) = \begin{cases} \infty & \text{if } s \notin [s_{min}, s_{max}] \text{ or } |\alpha| > \alpha_{max} \\ r|u - x_c| + r|v - y_c| & \text{else} \end{cases} \quad (7)$$

The model parameters $\Theta = (\alpha, \gamma, \delta, \rho, r)$ are learned in a supervised manner on the training set through a procedure described in Section 3.5.

One advantage of the generative model described in eq. (4) is that one could easily obtain samples from this model, by sampling the PCA coefficients β from the Gaussian prior $\beta \sim \frac{1}{Z_1} \exp(-E_p(\beta))$ and the deformation field \mathbf{d} from the Gaussian MRF $\mathbf{d} \sim \frac{1}{Z_2} \exp(-\sum_i \alpha_i d_i^2 + \sum_i \gamma_i (d_i - d_{i-1})^2)$. In Figure 5 are shown a few samples from the learned horse model with the PCA shape S shown in green and the sampled shape C in black.

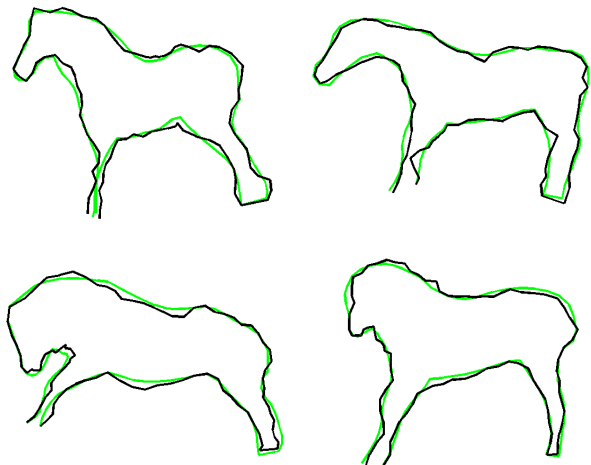


Figure 5. Sample shapes from the shape model (4) with the parameters of the learned horse model. PCA shape (green) and sampled shape (black).

3.2. Inference Algorithm

Finding the object parsing C and the PCA parameters (A, β) is a nontrivial optimization problem. However, if the PCA parameters (A, β) are known, the parsing C is uniquely determined by the displacement

vector $\mathbf{d} = (d_1, \dots, d_N)$, hence $C = C(\mathbf{d})$. In this case finding the optimal $C(\mathbf{d})$ is equivalent to finding \mathbf{d} that minimizes $E(C(\mathbf{d}), A, \beta) = E(\mathbf{d})$. This can be done efficiently by dynamic programming, due to the additive nature of the model when the PCA shape (A, β) is fixed

$$E(\mathbf{d}) = \sum_{i=1}^{N-1} \varphi(C_i, C_{i+1}) + \sum_i \alpha_i d_i^2 + \sum_i \gamma_i (d_i - d_{i-1})^2 + ct.$$

If the parsing C is fixed, an approximate minimum of $E(C, A, \beta)$ can be obtained by least square fitting of the PCA shape parameters (A, β) .

Therefore, if the PCA shape parameters (A, β) are initialized close to their optimal values, an approach that alternates the above two steps, namely the computation of the parsing C by dynamic programming and the estimation of the PCA parameters (A, β) by least squares, will converge to an approximate local optimum of $E(C, A, \beta)$ in a few iterations. This approach is similar in spirit to the Active Shape Model, with the difference that a consistent low energy deformation C is found by optimization in our method instead of finding data evidence on each normal independently as the ASM does.

We will use a data-driven approach described in Section 3.3 to find a number of candidate shapes $(A_i, \beta_i), i = 1, \dots, N^{cand}$ for initialization of the local optimum search described above. The final solution is obtained as the lowest energy configuration (C, A, β) among the N^{cand} local optima obtained. The whole optimization algorithm is described in Algorithm 1 below.

Algorithm 1 Optimization Algorithm

Input: Noisy point cloud e.g. edge detection image, PCA candidates $(A_i, \beta_i), i = 1, \dots, N^{cand}$.

Output: Near-optimal hidden variables $(\hat{C}, \hat{A}, \hat{\beta})$.

for $i = 1$ **to** N^{cand} **do**

for $j = 1$ **to** N_{iter} **do**

 Find displacement vector \mathbf{d} using dynamic programming

$$\mathbf{d} = \underset{\mathbf{d}}{\operatorname{argmin}} E_{data}(C(\mathbf{d})) + E(\mathbf{d}|A_i, \beta_i). \quad (8)$$

 Refit (A_i, β_i) by least squares on $C(\mathbf{d})$

end for

 Obtain $C_i = C(\mathbf{d})$.

end for

Find $j = \operatorname{argmin}_i E(C_i, A_i, \beta_i)$

Obtain $(\hat{C}, \hat{A}, \hat{\beta}) = (C_j, A_j, \beta_j)$

As the model energy (2) is just an approximation of the true object shape model, it is possible that other ways to combine the candidates such as weighted averaging [22] might be better than choosing the lowest energy one. This is subject to further investigation.

3.3. PCA Candidate Generation

The PCA shape candidates are obtained by matching one or more contour fragments to parts of the PCA model. The contour fragments are similar to [10, 21] and are obtained in a preprocessing step described in Section 3.4 below.

An initial set of PCA candidates can be obtained from one contour fragment, as described in Section 3.3.1. If more accuracy is desired, these initial candidates can be refined by matching other contour fragments near the candidates to other parts of the PCA model, as described in Section 3.3.2.

3.3.1 Candidate Generation from One Contour Fragment

These PCA candidates are obtained by matching a contour fragment to different parts of the PCA model. To speed-up computation, an interval $[L(l), U(l)]$ for the number of PCA points that match contour fragments of length l (made integer) is obtained from the training set and the ground truth annotations.

The method for obtaining the PCA candidates from one contour fragment is described in Algorithm 2.

Algorithm 2 CG1(N^{cand})

Input: Contour fragments c of length $len(c) \in [l_{min}, l_{max}]$

Output: At most N_1^{cand} different PCA shape candidates (A_i, β_i) with matches (c_i, b_i, k_i) .

for any contour fragment c **do**

for any k with $L(l) \leq k \leq U(l)$ where $l = len(c)$ **do**

 Subsample c evenly to have k points p_1, \dots, p_k .

for $1 \leq b \leq N$ **do**

 Fit points $b, \dots, b+k-1$ of PCA shape (A, β) to p_1, \dots, p_k in a least square sense.

 Discard (A, β) if the matching error is above a threshold.

end for

end for

end for

Perform Non-Max Suppression to keep at most N_1^{cand} candidates.

The Weighted PCA [19], described in the Appendix, is used to fit in a least square sense a given subset of a PCA shape to a number of points p_1, \dots, p_k .

The non-maximal suppression step finds the candidate of smallest fitting error and removes all candidates at average point-to-point distance at most D_1^{nms} from it, then adds the remaining candidate of smallest error, and so on.

For each obtained PCA shape candidate (A_i, β_i) , $i = 1, \dots, N_1^{cand}$ we also remember the contour fragment c_i and match location b_i, k_i that were used to generate it.

In Figure 6, left is shown the closest candidate to the ground truth among $N_1^{cand} = 200$ candidates obtained by Algorithm 2.

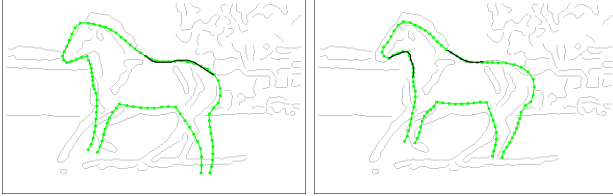


Figure 6. The best candidate obtained from one (left) and two (right) contour fragments. The fragments that generated each candidate are shown in black.

3.3.2 Candidate Generation from Two Contour Fragments

Usually images contain more than one contour fragment of the object to be segmented. We can refine a candidate obtained by **CG1** by fitting it simultaneously to the contour fragment it was obtained from and to another fragment close to the shape. Experiments in Section 4 show that this strategy can improve the quality of the candidates and of the final result. The details of this strategy are given in Algorithm 3.

Algorithm 3 CG2(N^{cand})

Input: PCA shape candidates (A_i, β_i) with matches (c_i, b_i, k_i) from **CG1** and contour fragments c .

Output: At most N^{cand} different PCA shape candidates (A_i, β_i) .

for $i = 1$ **to** N_1^{cand} **do**

Set $(P_1, \dots, P_N)' = S(A_i, \beta_i)$ from Eq. (1).

for any contour fragment c **do**

Find $P_j, P_k, 1 \leq j, k \leq N$ closest to the beginning and end of c

if $d(c, P_j) + d(c, P_k) < 2d^{max}$ and $[j, k]$ does not overlap with $[b_i, b_i + k_i - 1]$ **then**

Subsample c to have $m = k - j + 1$ points p_1, \dots, p_m .

Find PCA shape (A, β) that fits points $b_i, \dots, b_i + k_i - 1$ through c_i and j, \dots, k through p_1, \dots, p_m in a least square sense.

Discard (A, β) if the matching error is above a threshold.

end if

end for

end for

Perform Non-Max Suppression to keep at most N^{cand} candidates.

3.4. Preprocessing

Preprocessing begins with tracing the input points into point chains based on the 8-neighborhood. The point chains are then subsampled every 5-6 pixels to reduce the number of contour fragments obtained.

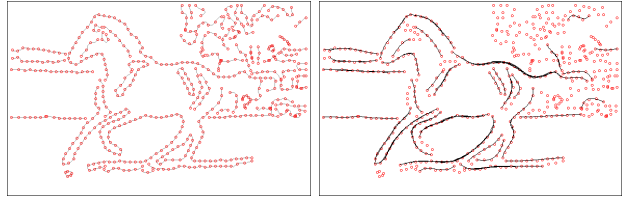


Figure 7. Left: the input points are traced into point chains and subsampled every 5-6 pixels. Right: smooth contour fragments (black) are fitted through the point chains starting and ending in the subsampled pixels.

The contour fragments used by the candidate generators are represented as a polynomials of degree three relative to a system of coordinates aligned with the contour's endpoints, as illustrated in Figure 8. The contour fragment endpoints are two of the subsampled points of the same traced point chain and the polynomial is fitted in a least square sense through all the chain points in between. The fragments are restricted in length to a range $[l_{min}, l_{max}]$. Only the fragments with a maximum error at most $e_{max} = 1.5$ are kept. Non-maximal contour fragments (based on the sets of chain points they were constructed from) are removed. An example of obtained contour fragments is shown in Figure 7, right.

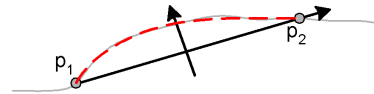


Figure 8. A contour fragment (red dashed) is a polynomial fit of a subset of a chain of points (shown in gray).

3.5. Learning the Model and Algorithm Parameters

The proposed model is very simple. It consists of a PCA model with at most 10 principal directions plus a small number (< 20) of parameters. Because the model is small, it should be expected that it generalize well to unseen data if the training data is representative.

The PCA model is learned in the standard way using Procrustes analysis to align the training shapes.

For the rest of parameters that need to be learned we adopt a supervised approach employed in other MRF-based methods [2, 16, 20], namely learning the parameters by optimizing a loss function on the training set. To speed-up the parameter learning, for candidate gen-

erators we employ loss functions that directly evaluate the generated candidates instead of the final result.

The parameters of the candidate generators are learned first, in the order **CG1** and **CG2**, using the minimum of the average point-to-point distances from the candidates to the ground truth annotation (described in Section 4) as loss function. This speeds-up the learning process since the **CG** parameters are this way decoupled from the later modules. Other measures, such as detection rate/false positive rate for the contour fragments, could be used instead and are subject to further investigation. The number of PCA components were fixed to $p = 4, 8$ for **CG1** respectively **CG2** except for the faces where they were $p = 2, 4$ for **CG1** respectively **CG2**.

We adopted a coordinate descent optimization (where one parameter is optimized at a time) and picked values that balance speed and accuracy. The obtained parameters for **CG1** are $l_{min} = 20, l_{max} = 60, N_1^{cand} = 200, D_1^{nms} = 5$, and $N^{cand} = 400, D^{nms} = 8, d^{max} = 20$ for **CG2**.

In Figure 9 are shown the average errors of the closest candidate obtained by **CG1-2** on the training and test sets vs the number of candidates N^{cand} .

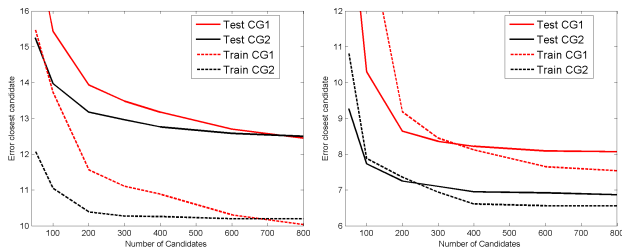


Figure 9. Candidate generator error vs. number of candidates for the horse (left) and cow (right) datasets.

Figure 9 shows that the test error decreases as the the training error decreases, which means that there is minimal overfitting for the candidate generators. Observe that **CG2** obtains better candidates than **CG1** (closer to the ground truth), especially for the cow images.

Similar behaviors were observed for the D_1^{nms}, D^{nms} parameters and for the d^{max} parameter of **CG2**.

The model parameters $\Theta = (\alpha, \gamma, \delta, \rho, r)$ are learned based on the average point-to-point distance between the obtained parsing results and the ground truth annotation.

$$Err(\Theta) = \frac{1}{n} \sum_{i=1}^n err_i(\Theta) \quad (9)$$

where $err_i(\theta)$ is the average point-to-point error of the parsing result obtained with parameters Θ on example i using **CG1**.

The model parameters $\delta, \rho, \alpha_i = \alpha, r, p$ were obtained by optimizing the error measure (9) on the training set by coordinate descent, with parameters $\gamma_i = 0.1, N_{iter} = 10$ fixed. The obtained values are given in Table 1.

Table 1. Learned parameters for Algorithm 1.

Dataset	α_i	δ	ρ	r	p
Weizmann horses [4]	0.04	2	2	1	10
Cows [13]	0.04	2	2	0.5	10
IMM Faces [24, 25]	0.04	7	2	0.5	6

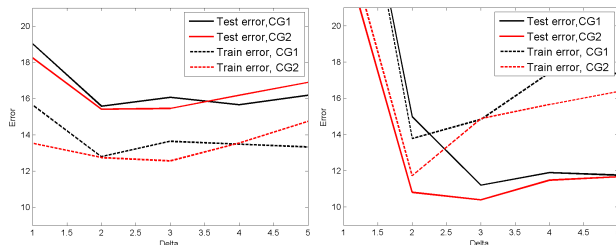


Figure 10. The parsing error measure (9) vs δ for the horses (left) and cows (right).

The dependence of the error on the values of δ and ρ are shown in Figure 10. Again, the test errors follow the training error.

4. Experimental Results

We evaluated this approach on three datasets: the Weizmann dataset [4] containing 328 horse images with object segmentations as binary masks, the Cows dataset [13] with 111 cow images and the IMM face dataset from [24, 25]. We used the same subsets of images as [31] for training and testing the Weizmann dataset and the first 25 images for training the Cows dataset and tested on all 111 images.

Each horse and cow were manually annotated with 14 control points on the boundary, as illustrated in Figure 11, left. For fairness, the same horse and cow legs were annotated as in [31]. Smooth curves were obtained between the control points by dynamic programming to minimize the average distance to the object boundary from the binary mask. Intermediate points were obtained by dividing the smooth curves into equal parts. The obtained annotation is shown in Figure 11, right, with 96-points for the horses and 87 points for the cows.

We also evaluated a standard Active Shape Model [6] initialized in the center of the image with average scale, no rotation $\theta = 0$ and 20 update iterations.

The results are summarized in Tables 2,3 and 4. In Fig. 12 are plotted the sorted errors on the datasets,

Table 2. Performance of different methods on the Weizmann Horse dataset.

Method	Train images	Test images	Contour points	Train error	Test error	Time/img (sec)
Active Shape Model [6]	50	227	96	25.35	29.05	<1
Recursive Compositional Models [31]	50	227	27	-	16.04	23
Ours, with CG1	50	227	96	12.79	15.58	44
Ours, with CG2	50	227	96	12.74	15.41	69
Ours, with CG2, no head or legs	50	227	60	8.21	11.42	20

Table 3. Performance of different methods on the Cows dataset.

Method	Train images	Test images	Contour points	Train error	Test error	Time/img (sec)
Active Shape Model [6]	25	111	87	48.81	49.23	<1
Recursive Compositional Models [31]	1	111	27	-	15.8	3.5
Ours, with CG1	25	111	87	13.78	14.98	14
Ours, with CG2	25	111	87	11.73	10.81	28

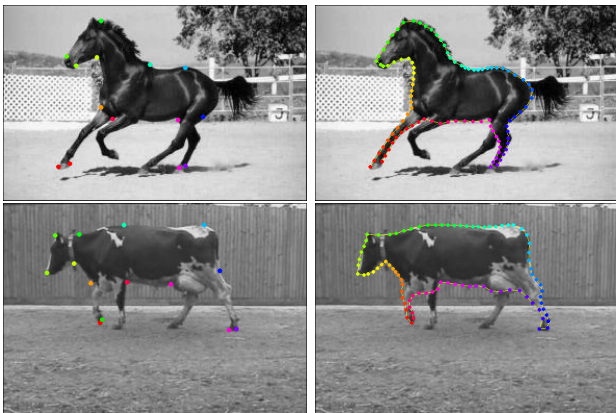


Figure 11. Left: each image is manually annotated with 14 control points and smooth curves (yellow) are obtained between the control points using the ground truth segmentation. Right: The obtained boundary annotation with 96 points (horses) and 87 points (cows).

from which different error percentiles can be obtained. The Recursive Compositional Model [31] also reports average point-to-point errors on the Weizmann and cow datasets but uses both edge and intensity information, unlike our approach, which only uses edge information.

We are not aware on any fully automatic face alignment results on the IMM face dataset [24]. The results published in [24] and other publications referring to this dataset initialize their algorithms at locations close to the true location and report the error after convergence.

The PCA model has difficulties modeling the shape variability of the horse head and legs. If the head and leg points are removed, the training and test errors decrease substantially, as it can be seen in the last row of Table 2. This experiment suggests that other shape

models with free parameters for the head and leg positions might be more appropriate than PCA for the higher level model. Such models are subject to further investigation.

Parsing examples using **CG2**, are shown in Figures 13,14,15 and 16.

5. Conclusion and Future Work

This paper presented a method for object parsing from noisy point clouds such as edge detection results. The object shape is modeled as a MRF deformation of a hidden PCA model. The model parameters are inferred by an algorithm that searches for the energy minimum through many local searches starting from a number of data-driven initializations. The experimental results show that our method is competitive with modern approaches for object parsing from point clouds such as the Recursive Compositional Models [31] and Active Shape Models [6].

The candidate generators and the parsing module can be easily parallelized, expecting a 10-100 times speedup from a GPU implementation.

In the future, we plan to investigate more accurate models for the higher level, with free parameters for the head and leg positions. We also plan to extend the method to 3D object parsing using approximate inference methods such as Graph Cuts or Belief Propagation for the boundary matching.

References

- [1] X. Bai, X. Wang, L. Latecki, W. Liu, and Z. Tu. Active skeleton for non-rigid object detection. In *ICCV*, pages 575–582, 2009.
- [2] A. Barbu. Training an Active Random Field for Real-Time Image Denoising. *IEEE Trans. Image Processing*, 18(11):2451–2462, 2009.

Table 4. Performance of different methods on the IMM Face dataset at 320×240 resolution.

Method	Train images	Contour points	Train error	Time/img (sec)
Active Shape Model [6]	240	58	21.73	<1
Ours, CG1	240	58	12.40	1.5
Ours, CG2	240	58	9.25	3

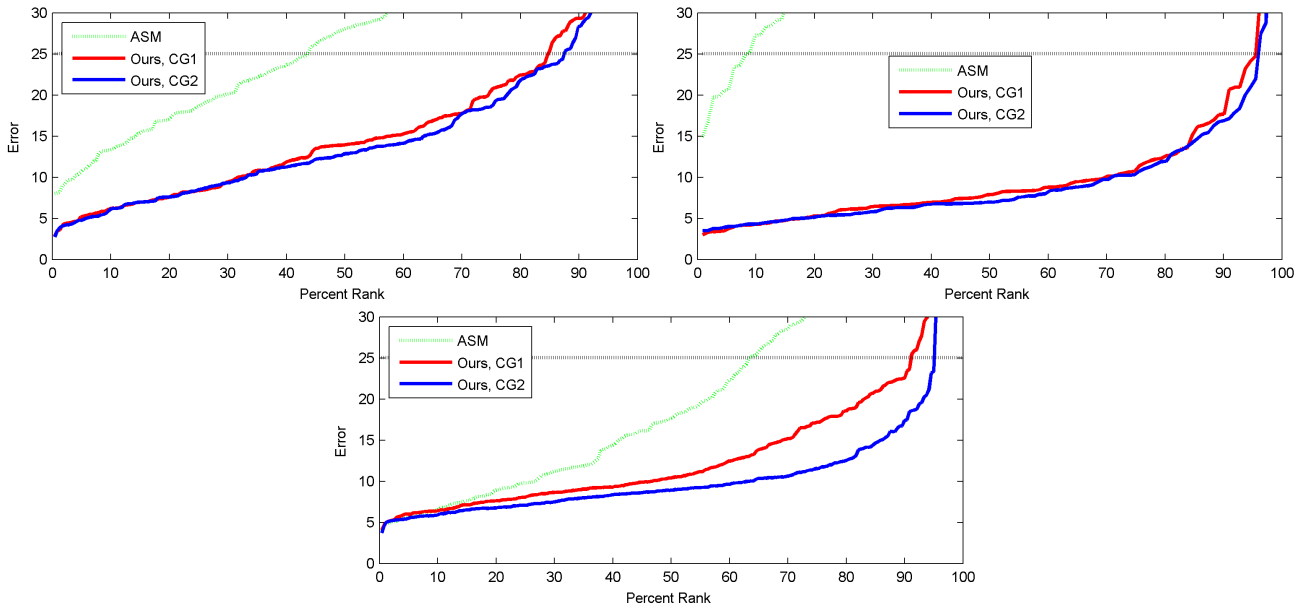


Figure 12. The sorted errors (9) of our algorithm on the 227 test images from the Weizmann dataset (top left), on the 111 images of the cow dataset (top right) and on the 240 images of the IMM face dataset (bottom).

- [3] A. Besbes, N. Komodakis, G. Langs, and N. Paragios. Shape priors and discrete mrfs for knowledge-based segmentation. In *Computer Vision and Pattern Recognition, 2009. CVPR 2009. IEEE Conference on*, pages 1295–1302. IEEE.
- [4] E. Borenstein and S. Ullman. Class-specific, top-down segmentation. *ECCV*, pages 639–641, 2002.
- [5] E. Borenstein and S. Ullman. Combined Top-Down/Bottom-Up Segmentation. *IEEE Trans. PAMI*, 30(12):2109–2125, 2008.
- [6] T. Cootes and C. Taylor. *Statistical Models of Appearance for Computer Vision*. 2001.
- [7] P. Dollar, P. Welinder, and P. Perona. Cascaded pose regression. In *CVPR*, pages 1078–1085, 2010.
- [8] P. Felzenszwalb and J. Schwartz. Hierarchical matching of deformable shapes. In *CVPR*, 2007.
- [9] L. Fernandes and M. Oliveira. Real-time line detection through an improved Hough transform voting scheme. *Pattern Recognition*, 41(1):299–314, 2008.
- [10] V. Ferrari, L. Fevrier, F. Jurie, and C. Schmid. Groups of adjacent contour segments for object detection. *IEEE Trans. PAMI*, pages 36–51, 2007.
- [11] V. Ferrari, F. Jurie, and C. Schmid. From Images to Shape Models for Object Detection. *IJCV*, 87(3):284–303, 2010.
- [12] D. Freedman and T. Zhang. Interactive graph cut based segmentation with shape priors. In *CVPR 2005*, volume 1, pages 755–762. IEEE.
- [13] B. Leibe, A. Leonardis, and B. Schiele. Combined object categorization and segmentation with an implicit shape model. In *Workshop on Statistical Learning in Computer Vision, ECCV*, pages 17–32, 2004.
- [14] A. Levin and Y. Weiss. Learning to combine bottom-up and top-down segmentation. *IJCV*, 81, 2009.
- [15] Y. Li, L. Gu, and T. Kanade. A robust shape model for multi-view car alignment. In *CVPR*, 2009.
- [16] Y. Li and D. P. Huttenlocher. Learning for optical flow using stochastic optimization.
- [17] J. Malcolm, Y. Rathi, and A. Tannenbaum. Graph cut segmentation with nonlinear shape priors. In *Image Processing, 2007. ICIP 2007. IEEE International Conference on*, volume 4, pages IV–365. IEEE, 2007.
- [18] X. Ren, C. Fowlkes, and J. Malik. Cue integration for figure/ground labeling. *NIPS*, 18:1121, 2006.
- [19] M. Rogers and J. Graham. Robust active shape model search. *ECCV*, pages 289–312, 2006.
- [20] D. Scharstein and C. Pal. Learning conditional random fields for stereo. In *CVPR*, pages 1–8, 2007.
- [21] J. Shotton, A. Blake, and R. Cipolla. Multi-Scale Categorical Object Recognition Using Contour Fragments. *IEEE Trans. PAMI*, 2008.

- [22] M. Sofka, J. Zhang, S. Zhou, and D. Comaniciu. Multiple object detection by sequential monte carlo and hierarchical detection network. In *Computer Vision and Pattern Recognition (CVPR), 2010 IEEE Conference on*, pages 1735–1742. IEEE.
- [23] M. Stark, M. Goesele, and B. Schiele. A shape-based object class model for knowledge transfer. In *ICCV*, pages 373–380, 2010.
- [24] M. B. Stegmann. Analysis and segmentation of face images using point annotations and linear subspace techniques, 2002.
- [25] M. B. Stegmann, B. K. Ersbøll, and R. Larsen. FAME – a flexible appearance modelling environment. *IEEE Trans. on Medical Imaging*, 22(10):1319–1331, 2003.
- [26] L. Torresani, A. Hertzmann, and C. Bregler. Learning non-rigid 3d shape from 2d motion. In *NIPS*, 2003.
- [27] A. Toshev, B. Taskar, and K. Daniilidis. Object detection via boundary structure segmentation. In *CVPR*, pages 950–957, 2010.
- [28] J. Winn and N. Jojic. Locus: Learning object classes with unsupervised segmentation. In *ICCV*, 2005.
- [29] Y. Wu, Z. Si, H. Gong, and S. C. Zhu. Learning active basis model for object detection and recognition. *IJCV*, pages 1–38, 2009.
- [30] X. Yang, T. Wu, and S. C. Zhu. Evaluating information contributions of bottom-up and top-down processes. In *ICCV*, pages 1042–1049, 2010.
- [31] L. Zhu, Y. Chen, and A. Yuille. Learning a hierarchical deformable template for rapid deformable object parsing. *IEEE Trans. PAMI*, 2009.
- [32] Q. Zhu, G. Song, and J. Shi. Untangling cycles for contour grouping. In *ICCV*, pages 1–8. IEEE, 2007.

Appendix: Weighted PCA

A partial PCA model can be fit to a number of points using the weighted least squares method [19], summarized in Algorithm 4. The weights of missing PCA points are set to zero. The weighted alignment between the shapes S_1, S_2 has been described in Appendix C from [6].

Algorithm 4 FitWeightedPCA

Input: Shape $S_1 = (\mathbf{x}_1, \mathbf{y}_1)$, weight vector $\mathbf{w} = (w_1, \dots, w_N)'$, $\|\mathbf{w}\|_1 = \sum_{i=1}^N w_i = 1$.

Output: Weighted least-square fit parameters (A, β)

Set $W = \text{diag}(w_1, \dots, w_N)$

Set $K_x = (P_x'W^2P_x)^{-1}P_x'W^2$, $K_y = (P_y'W^2P_y)^{-1}P_y'W^2$

Set $\beta = 0$

for $i = 1$ **to** N_{it} **do**

Set $S_2 = (\mathbf{x}_2, \mathbf{y}_2)$, $\mathbf{x}_2 = \mu_x + P_x\beta$, $\mathbf{y}_2 = \mu_y + P_y\beta$

Solve

$$\begin{pmatrix} S_{xx} + S_{yy} & 0 & S_x & S_y \\ 0 & S_{xx} + S_{yy} & -S_y & S_x \\ S_x & -S_y & S_w & 0 \\ S_y & S_x & 0 & S_w \end{pmatrix} \begin{pmatrix} a \\ b \\ dx \\ dy \end{pmatrix} = \begin{pmatrix} S_1 \\ S_2 \\ \mathbf{x}'_2\mathbf{w} \\ \mathbf{y}'_2\mathbf{w} \end{pmatrix}$$

with $S_x = \mathbf{x}'_1\mathbf{w}$, $S_y = \mathbf{y}'_1\mathbf{w}$, $S_w = \|\mathbf{w}\|_1 = 1$

$S_{xx} = \mathbf{x}'_1W\mathbf{x}_1$, $S_{yy} = \mathbf{y}'_1W\mathbf{y}_1$

$S_1 = \mathbf{x}'_1W\mathbf{x}_2 + \mathbf{y}'_1W\mathbf{y}_2$

$S_2 = \mathbf{y}'_1W\mathbf{x}_2 - \mathbf{x}'_1W\mathbf{y}_2$

Obtain $A(\mathbf{x}, \mathbf{y}) = (a\mathbf{x} + b\mathbf{y} + dx, -b\mathbf{x} + a\mathbf{y} + dy)$

Find $(\mathbf{x}_o, \mathbf{y}_o) = A^{-1}(S_1)$

Set $\beta = K_x(\mathbf{x}_o - \mu_x) + K_y(\mathbf{y}_o - \mu_y)$

end for

Set $s = \sqrt{a^2 + b^2}$, $\theta = \arctan(b/a)$.

Obtain $A = (dx, dy, s, \theta)$

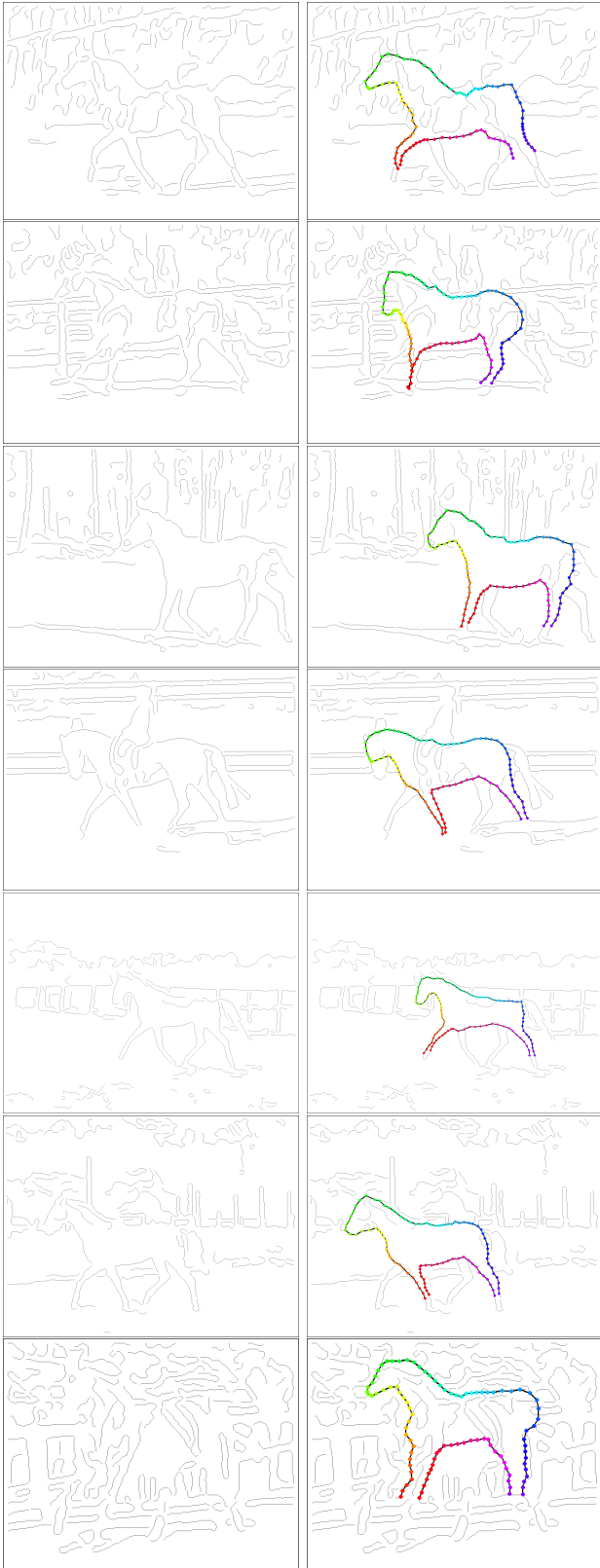


Figure 13. Results on test set. Left: Traced points. Right: parsing result (black) with associated PCA shape (green).

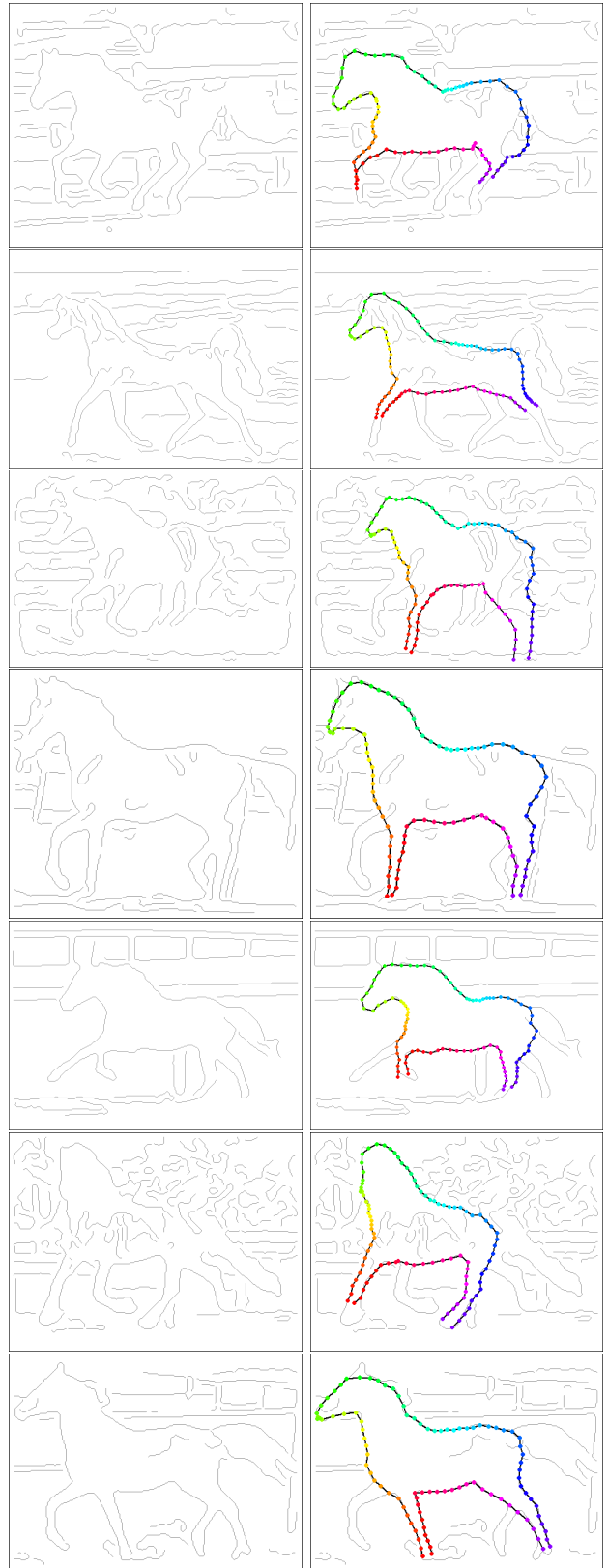


Figure 14. More results on test set.

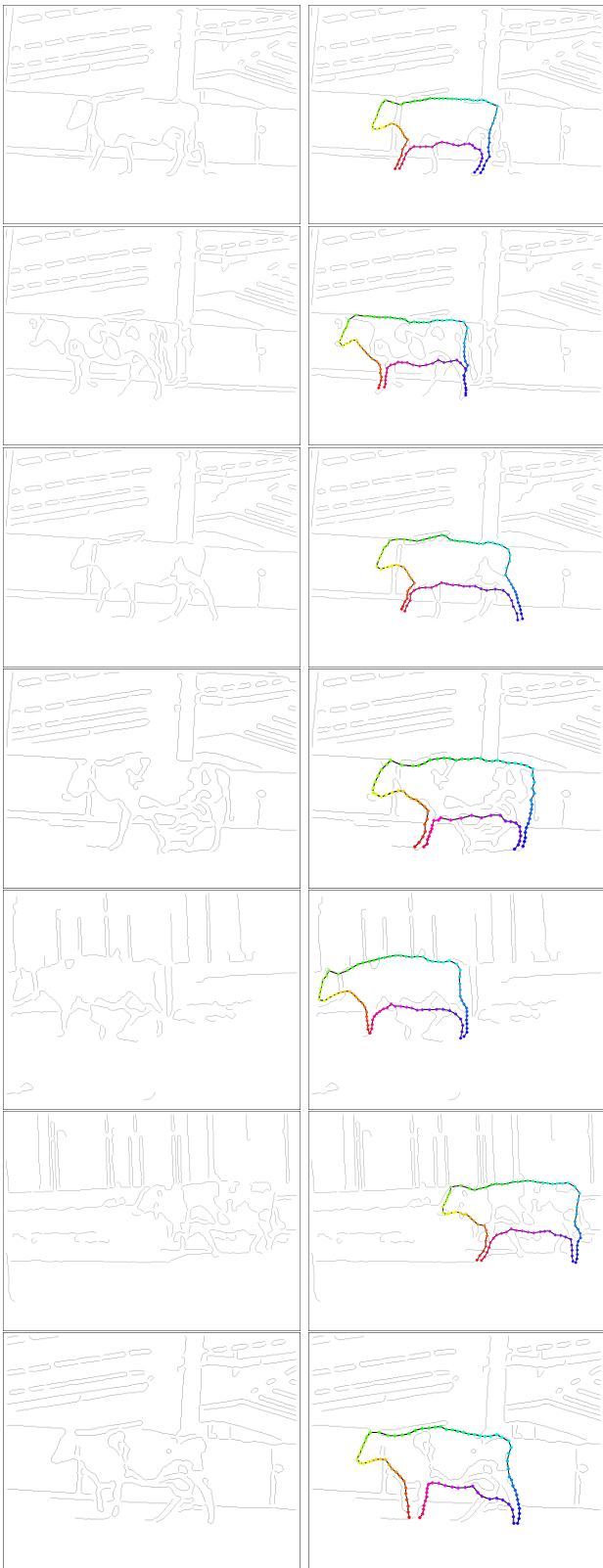


Figure 15. Results on the cow dataset.

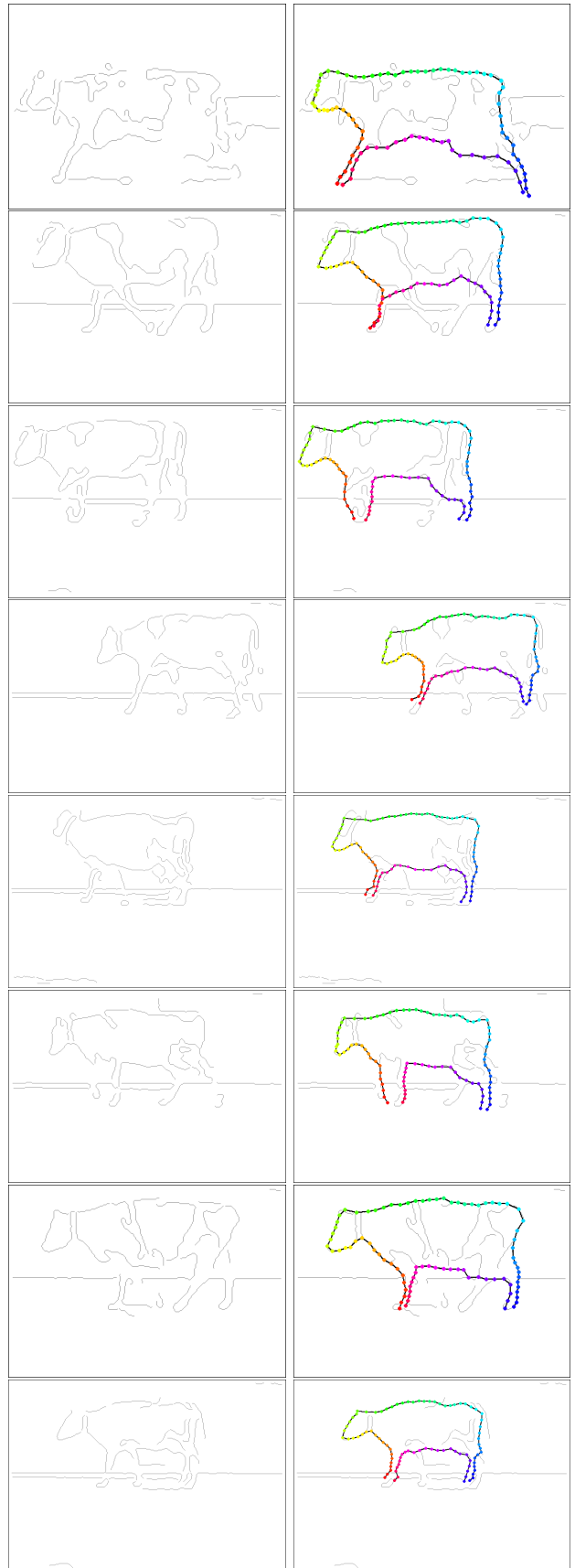


Figure 16. More results on the cow dataset.